# Highly motile nanoscale magnetic artificial cilia

Tanveer ul Islam[a,b], Yves Bellouard[b], and Jaap M. J. den Toonder[a,c,1]

[a]Microsystems Section, Mechanical Engineering, Eindhoven University of Technology, 5612 AZ Eindhoven, the Netherlands; [b]Galatea Laboratory, Institute of Electrical and Microengineering, School of Engineering, Ecole Polytechnique Fédérale de Lausanne (EPFL), CH-2002 Neuchâtel, Switzerland; and [c]Institute for Complex Molecular Systems, Eindhoven University of Technology, 5612 AZ Eindhoven, the Netherlands

Edited by Kenneth Breuer, Brown University, Providence, RI, and accepted by Editorial Board Member Joanna Aizenberg July 24, 2021 (received for review March 17, 2021)

**Among the many complex bioactuators functioning at different scales, the organelle cilium represents a fundamental actuating unit in cellular biology. Producing motions at submicrometer scales, dominated by viscous forces, cilia drive a number of crucial bioprocesses in all vertebrate and many invertebrate organisms before and after their birth. Artificially mimicking motile cilia has been a long-standing challenge while inspiring the development of new materials and methods. The use of magnetic materials has been an effective approach for realizing microscopic artificial cilia; however, the physical and magnetic properties of the magnetic material constituents and fabrication processes utilized have almost exclusively only enabled the realization of highly motile artificial cilia with dimensions orders of magnitude larger than their biological counterparts. This has hindered the development and study of model systems and devices with inherent size-dependent aspects, as well as their application at submicrometer scales. In this work, we report a magnetic elastomer preparation process coupled with a tailored molding process for the successful fabrication of artificial cilia with submicrometer dimensions showing unprecedented deflection capabilities, enabling the design of artificial cilia with high motility and at sizes equal to those of their smallest biological counterparts. The reported work crosses the barrier of nanoscale motile cilia fabrication, paving the way for maximum control and manipulation of structures and processes at micro- and nanoscales.**

magnetic elastomer | nano artificial cilia | extreme deflection | high-frequency actuation

Described as the "surprise organelle" of the first decade of the twenty-first century, the hair-like microscopic structure cilium remains as intriguing as at the time of its discovery (1, 2). Just a few micrometers long and some hundreds of nanometers thick, cilia perform a wide range of vital functions in our body as chemo- and mechanosensors (3, 4) and as actuators (2). Efforts made to artificially mimic their functions have demonstrated and further pointed toward a broad range of applications in major areas like microfluidics (5–12), micro- and nanorobotics (13), cell and particle manipulation (14–16), surface enhancements (17), and many more. Fabrication of artificial cilia to act as actuators has triggered the use and development of various materials responsive to external stimuli like electric fields, chemicals, light, and magnetic fields (18–20). Less implemented methods involving pneumatic (21), acoustic (22), piezo (23), and mechanical (24) actuation have also been reported. Toward exercising a high degree of control and actuation, the implementation of magnetic materials offers a promising approach, in particular due to the noninteracting nature of magnetic fields with biological fluids and cells (25–27). As magnetic biomimetic microactuators are remotely addressable and reversible in short response times, their use enjoys an overwhelming acceptance in the biomimicry of organelle–cilia and many other bioprocesses (28, 29).

The magnetic materials investigated for artificial cilia so far are responsive hybrid composites known as magnetorheological elastomers (also referred to as magnetic elastomers) (30), which have magnetic particles embedded in an elastic polymer matrix. First developed for their field-dependent material properties, most importantly their tunable modulus (31), and to study the combined influence of magnetic field and elastic stresses in an elastomer (32), they quickly gained a lot of attention after a quasistatic model explaining their changing modulus was developed (33). Materials were further developed to enhance the field-dependent modulus by using magnetic particles with higher magnetization saturation values like the commonly used iron carbonyl particles. Magnetic artificial cilia with large sizes (i.e., lengths of hundreds of micrometers or more) have been successfully fabricated and demonstrated, but the fabrication of highly motile artificial cilia with submicrometer dimensions to faithfully mimic their biological counterparts has remained an open challenge due to a number of unresolved issues. First, magnetic particles most used in creating artificial cilia such as iron carbonyl and other magnetic particles have diameters of the order of a few micrometers (34), and the corresponding magnetic elastomers are therefore not suitable for fabricating artificial cilia with submicrometer dimensions. The magnetic artificial cilia we demonstrated earlier make use of these materials and therefore, have large diameters and lengths of tens and hundreds of micrometers or more, respectively (11, 35) (i.e., more than an order of magnitude larger than biological cilia). Conversely, magnetic elastomers with nanomagnetic particles have been less explored because of their much lower magnetization values and critical preparation processes. Complications in their preparation arise due to the presence of magnetic dipole moments and van der Waals forces existing between the nanoparticles, which

## Significance

**Cilia are hair-like microscopic structures present abundantly in our body and producing motions at the smallest scales. They perform a wide range of critical functions and are crucial for the normal functioning of our body. Abnormal functioning of cilia results in a number of diseases jointly known as ciliopathies. Artificially mimicking cilia is aimed at understanding their normal/abnormal functionality and at developing cilia-inspired micro-/nanoengineering devices. In this study, we present a magnetic polymer preparation process yielding a material with optimum properties and a cilia fabrication method producing the smallest highly motile artificial cilia with sizes equal to their biological counterparts. This opens avenues for biological studies and for creating submicrometer manipulation and control.**

Author contributions: T.u.I., Y.B., and J.M.J.d.T. designed research; T.u.I. performed research; T.u.I. analyzed data; and T.u.I., Y.B., and J.M.J.d.T. wrote the paper.

The authors declare no competing interest.

This article is a PNAS Direct Submission. K.B. is a guest editor invited by the Editorial Board.



[1]To whom correspondence may be addressed. Email: j.m.j.d.toonder@tue.nl.

This article contains supporting information online at https://www.pnas.org/lookup/suppl/doi:10.1073/pnas.2104930118/-/DCSupplemental.

Published August 27, 2021.

heavily hamper their dispersion in an elastomer without agglomeration (36). Reduction in particle–particle interaction, and therefore, the particle agglomeration, is attained by coating them with a layer of polymer, but this limits the maximum particle concentration possible to attain in the elastomer (25). Consequently, artificial cilia fabricated with lower concentration of particles in an elastomer show a lower degree of response, making them less effective in use (25). Cilia-like nanostructures fabricated from the only magnetic elastomers with sufficiently high particle concentration and nanoscale homogeneity (37) have also shown a limited bending response (27, 38). Recently, highly responsive cilia with nanoscale dimensions fabricated from nanomagnetic particle chains have been reported (39); a drawback from this approach is that the cilia dimensions and properties are limited by the particles available. In this study, we report a material preparation process for preparing a magnetic elastomer that overcomes these issues and is suitable for fabricating highly responsive micro-/nanostructures. Another limiting factor that hampers creating small-scale cilia is the fabrication process for which conventional mold and release processes are often used, using molds made with photolithography (11, 35). This limits the downscaling and aspect ratio of the cilia. To resolve these limitations, we further report a robust micro-/nanomolding process to shape and successfully release the micro-/nanocilia structures from their template. The material preparation method coupled with the tailored fabrication process enables us to make a major step and realize artificial structures faithfully mimicking the highly motile cilia at sizes equivalent to the smallest sizes found in nature. The fabricated artificial cilia we report here have radii and lengths down to 200 nm and 6 μm, respectively, and show a maximum possible bending angle of $90^0$ under an external magnetic field generated by a conventional magnet. This extremely large bending response is further exploited to demonstrate a complex $360^0$ rotary motion at large bending angles and at very high frequencies (up to 80 Hz) without loss of motility.

## Results and Discussion

The complete fabrication process consists of two main steps: first, synthesizing superparamagnetic nanoparticles followed by their coating and dispersion in a low–molecular weight polymer to yield a ferrofluid (Fig. 1*A*) and second, molding, in which the material is shaped, solidified, and released to obtain nanoscale cilia with desired properties (Fig. 1 *B*–*F*). The magnetic elastomer preparation process begins with synthesizing nanomagnetic particles from ferric and ferrous chloride salts in an alkaline aqueous solution, yielding particles of around 12 nm in size (25, 40). The pH of the alkaline solution could be raised to a high value of 12 while the particles remain suspended in the solution. The synthesized magnetite nanoparticles are known to bind under certain conditions with a polymer containing $6-7$ mol % aminopropylmethylsiloxane with dimethylsiloxane

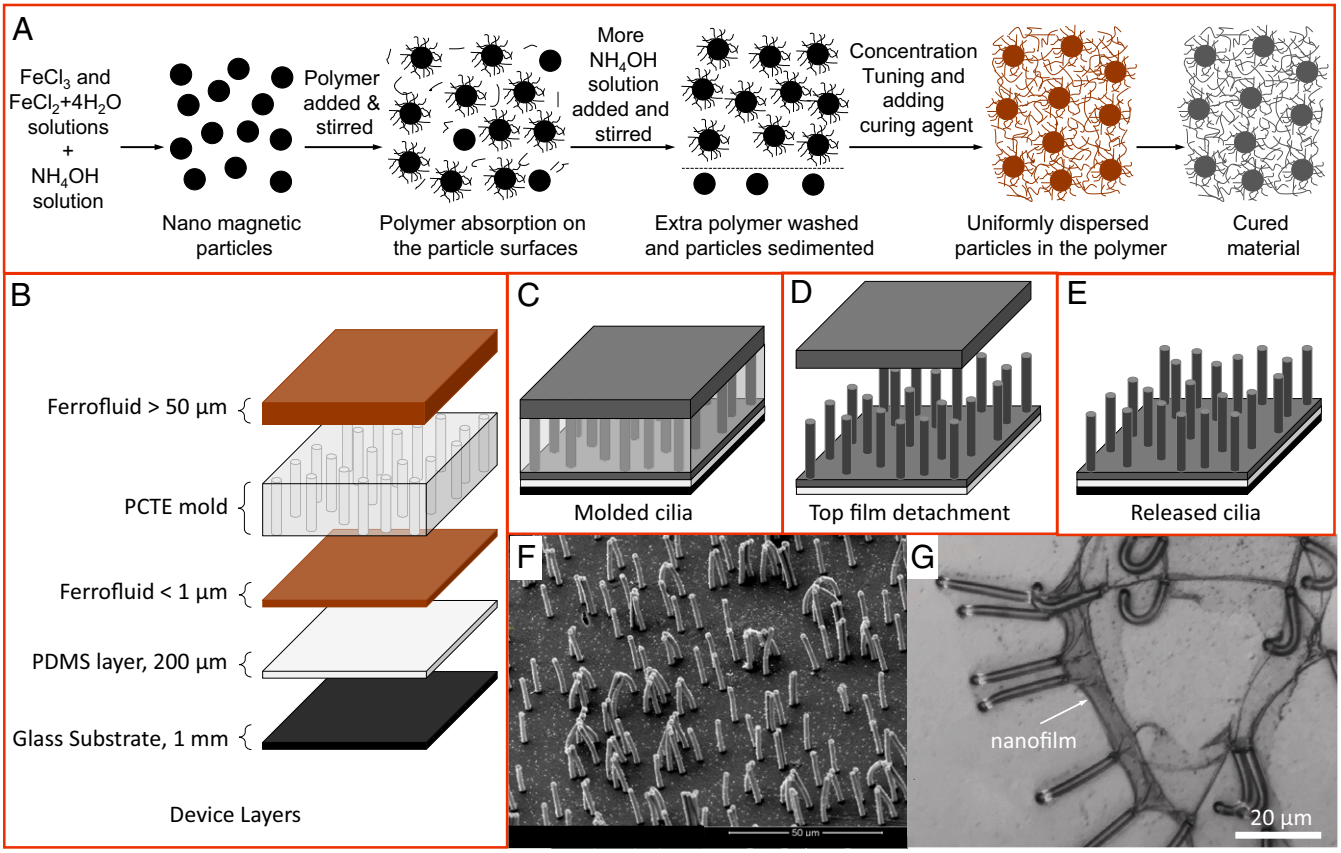


**Fig. 1.** Schematics of the ferrofluid preparation and molding process. (*A*) The particle synthesis process, their complexion with a polymer, extraction of the coated particles, and concentration tuning to yield a ferrofluid followed by its curing to form the elastomer are shown here. The particle coating efficiency of the process is above 95% (a detailed description is given in *Materials and Methods*). (*B*) Different layers of the device, their typical thicknesses, and the order of stacking. (*C*) Molded device configuration before and after curing as the curing only changes the liquid ferrofluid into a solid elastomer. (*D*) Top-layer detachment while washing; the glass substrate is removed before washing. (*E*) Released cilia attached to a glass substrate again. (*F*) Scanning electron microscopy image of fabricated artificial cilia; each cilium has a nominal radius of 1 μm and a length 23 μm. Cilia density is = $1 \times 10^6$ cm$^{-2}$. (*G*) Cilia fabricated without the addition of the top ferrofluid layer show a ruptured nanofilm attached to the cilia tips, which would trap and constrain cilia movement during the actuation process.

(AMS-162 from Gelest) (37). A specific procedure involving the use of aqueous ammonium hydroxide is adopted to create the right pH conditions for the particle to bind with the added polymer. The coated particles are cleanly extracted using the solvents methanol and water in a particular manner to be further tuned to different concentrations. The setup designed for the material preparation process, the procedure adopted for the particle coating, the steps followed for extracting coated particles, and the final ferrofluid preparation are discussed in detail in *Materials and Methods*. The material preparation process allows particle concentration tuning from 0 to a maximum of around $50\,\mathrm{wt}\%$. Higher concentration of particles with magnetization $\mathrm{M}$ present in a material with Young's modulus $E$ and density $\rho$ favors large bending angles $\theta$ (relative to the normal to the surface) of a cilium structure present in a free space with magnetic permeability $\mu_0$, as $\theta$ is directly proportional to the quantity $\mu_0 M^2 \rho^2 / E$ (37). Although a maximum of $50\,\%$ particle concentration could be achieved, a concentration larger than $40 \pm 2\,\mathrm{wt}\%$ increases the ferrofluid's viscosity before curing in the molding process to such an extreme value that the material prematurely changes to a solid phase. At concentrations lower than $40 \pm 2\,\mathrm{wt}\%$, the material has enough fluidity before curing and optimal $E$ after curing required for the maximum deflection of fabricated micro- and nano-sized cilia structures. An adverse but unavoidable property that gets seeded in the prepared material is its reduced ultimate tensile stress. Lower ultimate stress restricts its use in most of the micro-/nanomolding processes involving a commonly used liftoff step to release structures from their templates. A second adverse property of the material is its high curing temperature of $130 - 180^0\mathrm{C}$, which affects the polycarbonate track etched (PCTE) membranes used as a mold for fabricating submicrometer artificial cilia, as detailed below. High temperature exposure modifies the PCTE mold such that it develops resistance to solvents like dimethyl sulfoxide otherwise used to dissolve it. Although sensitive to high temperatures, the PCTE mold is still selected for its defect-free and highly precise pore dimensions ranging from nano- to microscales. The molding process discussed next circumvents these issues to enable the cilia fabrication and actuation at their lowest size limits.

The molding process involves insertion of ferrofluid assisted by capillary action into the pores of the PCTE mold supported on a solidified polydimethylsiloxane (PDMS) layer (Fig. 1 *B* and *C*). A thin layer ($< 1\,\mu\mathrm{m}$) of ferrofluid is left between the PDMS layer and the PCTE mold, and an extra thick layer ($> 50\,\mu\mathrm{m}$) of ferrofluid is laid on top of the PCTE mold (Fig. 1*B*). Solidification/curing of the ferrofluid, in the molding process, is carried out by heating the sample in a vacuum oven that exposes the PCTE mold to a maximum temperature of $130^0\mathrm{C}$ while applying a magnetic field of $0.15 - 0.2\ T$ directed along the cilia length using permanent magnets to assist particle alignment. To remove the heat-modified etch-resistant PCTE mold, washing in anhydrous chloroform solvent ($\geq 99\%$, contains $0.5 - 1.0\%$ ethanol as stabilizer from Sigma-Aldrich) is found to completely remove the mold due to the comparable cohesive energy density of the PCTE and the solvent expressed in terms of solubility parameter or Hildebrand value (41). Use of solvents with polymers made from dimethylsiloxane, used in most of the soft lithography processes, is known to result in swelling problems with a swelling ratio of 1.39 in the chloroform solvent (41). The magnetic elastomer matrix, being a copolymer of dimethylsiloxane, shows a large and quick swelling in the solvent chloroform; it is found to first swell and wrinkle and then, may disintegrate the cured elastomer and therefore, the released cilia structures, but this is avoided by the presence of the PDMS layer (Fig. 1 *C* and *D*). Cilia grown on the freely standing PDMS layer of appropriate thickness allows equal swelling of the entire device as the measured swelling ration of $1.38 \pm 0.01$ of the magnetic elastomer is equivalent to the PDMS swelling, thus avoiding stress generation and therefore, the disintegration. Furthermore, in the absence of the top ferrofluid layer, a thin layer of tens of nanometers thickness (nanofilm) of the cured ferrofluid is observed to have settled on top of the membrane (Fig. 1*G*). Removal of the nanofilm is achieved by adding the extra ferrofluid layer on top of the PCTE mold, which mixes with the nanofilm while curing, thus increasing its net thickness. During washing, on exposure to the solvent chloroform, the thick film on the top quickly swells first, inducing enough stress to detach itself from the cilia tips and leaving the free cilia attached to the base behind (Fig. 1 *D*–*F*). Without the thick top ferrofluid layer, the nanofilm lacks the stiffness required to generate enough stress to detach itself from the cilia tips. Since the fabrication process involves the use of flat PCTE molds, the released cilia structures are formed over an extensively large flat surface compared with their sizes. This configuration allows clear visualization of the top view of the cilia structures at high magnifications, and only in limiting cases, the cilia devices are further modified to access the side view of the structures. The complete molding process involves the preparation of the substrate, curing of ferrofluid by following a specific heating profile, bonding and debonding of layers in a particular manner/sequence before and after washing, and finally, transferring the released cilia to a chip, keeping the cilia permanently immersed in a fluid medium (*SI Appendix*, Text S1 and Fig. S1). The cilia were preserved and studied while being immersed in ethanol, since this fluid is compatible with the chloroform used for washing. Also, ethanol has a low viscosity (similar to water) and it wets the polymer surface.

To demonstrate the successful use of the developed fabrication process for a broad range of micro- and nanoscale cilia structures, we selected four cilia sizes: cilia with nominal radii $(r)$ of 1.5 and 1 μm falling in the microrange and cilia with $r = 350$ and $200\,\mathrm{nm}$ falling in the nanoscale, all having a high aspect ratio between 11 and 15 and sufficiently spaced to avoid the interference of neighboring magnetic cilia (Fig. 2 and *SI Appendix*, Fig. S2).

After the successful fabrication of the cilia, their responsive behavior is analyzed by observing the cilia deformation induced by an applied magnetic torque. Both top-view and side-view observations are done, while the magnetic torque is applied using a permanent magnet positioned at varying locations relative to the cilia to change the magnitude of the applied torque. The concentration of magnetic particles is kept at $40 \pm 2\,\mathrm{wt}\%$. Fig. 3*A* illustrates the experimental configuration for the top-view measurements. The cilium deflection angle $\theta$ is determined from the observed projected cilia length and assuming that the cilium remains straight. Both the selected micro- and nanocilia show a deflection of 0 to $90^0$ as the lateral distance $x$ approaches zero (Fig. 3 *B* and *C*) since they tend to align to the magnetic field due to the magnetic torque. The observed bending behavior is compared with a model that balances the induced magnetic torque $(\tau_{mag})$ with the opposing deformation torque $(\tau_{def})$ acting on cilium structure (26). The magnetic torque is given by

$$\tau_{mag} = \frac{\nu |n_r - n_a|}{2\mu_0 n_a n_r} |B|^2 \sin(2(\theta - \phi)), \qquad [1]$$

which assumes that the magnetic field gradient is negligible, and that the induced magnetic moment is determined by the aspect ratio of the structure. The latter holds if the magnetic susceptibility is high, which is typical for the soft magnetic magnetite we have (26, 42). In the above expression, $\nu$ is the total volume of magnetic particles; $n_a$ and $n_r$ are the geometry demagnetization factors along and perpendicular to the cilium long axis, respectively; and $B$ is the magnitude of magnetic field vector $\overrightarrow{B}$ making an angle $(\phi - \theta)$ with the long axis of the

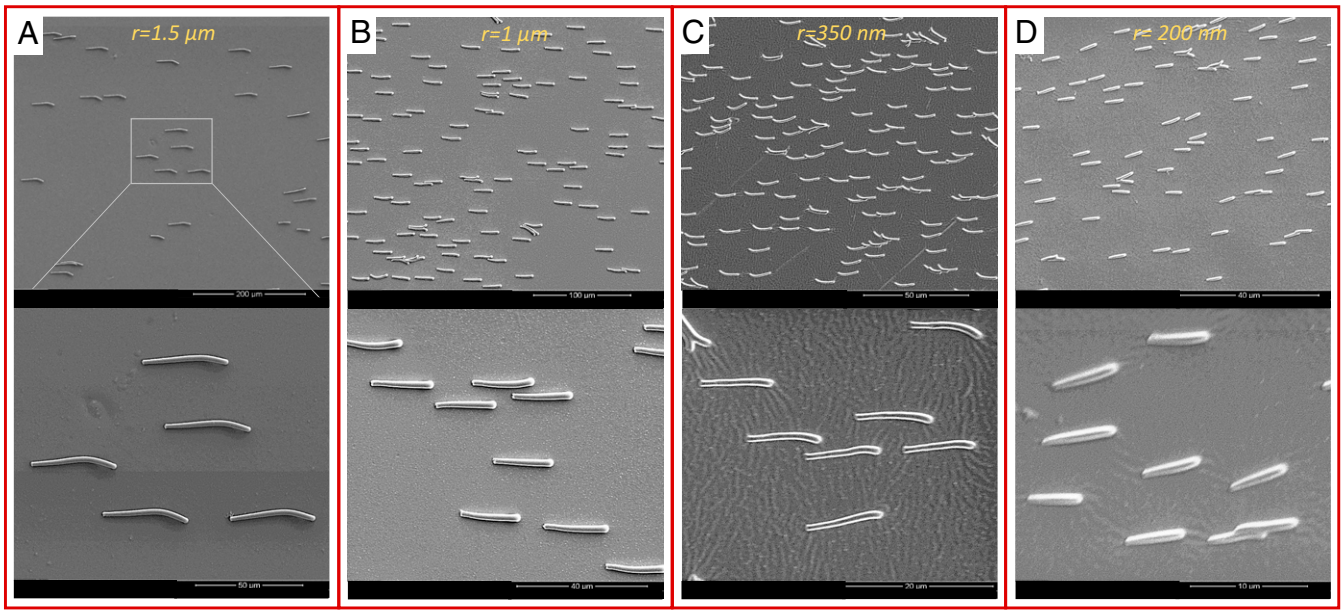


**Fig. 2.** Scanning electron microscopy images of micro- and nanocilia. (*A*) Microcilia with $r = 1.5$ μm, $L = 47$ μm, and density $=1 \times 10^4$ cm$^{-2}$. Images are made at different magnifications. (*B*) Microcilia with $r = 1$ μm, $L = 23$ μm, and density $= 1 \times 10^5$ cm$^{-2}$. (*C*) Nanocilia with $r = 350$ nm, $L = 9$ μm, and density $= 7 \times 10^5$ cm$^{-2}$. (*D*) Nanocilia with $r = 200$ nm, $L = 6$ μm, and density $= 1 \times 10^6$ cm$^{-2}$. All the cilia are fabricated and aligned in one direction by applying an external magnetic field while drying them in the ambient conditions.

cilium. $\tau_{mag}$ is balanced by the counteracting deformation torque given by

$$\tau_{def} = \frac{\pi E r^4 \theta}{L}, \qquad [2]$$

where $r$ is the cilium radius and $L$ is its length (26). Eq. **2** assumes that the cilium bends with a constant radius of curvature while undergoing large deformation; these assumptions induce a maximum 30% error in the predicted bending angle (25). The different parameters involved in these equations are measured or computed using different setups and tools (*SI Appendix*, Text S2 and Fig. S3). By minimizing the expression $\tau_{mag} + \tau_{def}$ against the only unknown parameter $\theta$ using a MATLAB code, the net bending angle $(\theta)$ is calculated as a function of $x$. Calculated results for both micro- and nanocilia agree very well with the experimental results within the 30% model accuracy (Fig. 3 *D* and *E*). The associated magnetic and deformation torques, according to the model, are shown in *SI Appendix*, Fig. S4 *C* and *D*. The model can be applied to estimate the bending response as a function of cilia aspect ratio (since this determines the induced magnetic moment), as shown in *SI Appendix*, Fig. S4*E* for the configuration of Fig. 3*D*. For an aspect ratio of 48, the cilium bending angle is optimally aligned with the magnetic field for all $x$, but our experimental cilia with a maximum aspect ratio of 16 are close to this optimum for smaller $x$.

For cilia viewed from the side, the permanent magnet arrangement is shown in Fig. 3*F*. Here, the field lines are always perpendicular ($\phi = 90^0$) to the initial direction of the cilia long axis. In this configuration, the cilia bend toward the field lines due to magnetic torque, with maximum bending as the distance $x$ approaches zero since then the magnetic field strength is largest, resulting in the largest torque (Fig. 3 *F* and *G*). Taking the cilia tip direction as the effective bending angle in this experiment, as indicated in Fig. 3, the cilia show a bending of around $80^0$ when the magnet is at $x = 0.5$ mm (Fig. 3*H*). The theoretical prediction of the cilia bending angle (based on Eqs. **1** and **2**) reasonably predicts the observed behavior, within the 30% model accuracy. Movie S3 shows the bending with decreasing $x$. The bending angle can be further increased to $90^0$ and beyond, by rotating the applied field direction. This is shown in Movie S4 for an experiment in which the permanent magnet is rotated around the cilium (at $x = 1.5$ mm), which enables bringing the cilia tips in touch with the base surface. The side view of the nanocilia undergoing large bending by bringing the magnet closer in steps is shown in Movie S5.

The maximum bending response of artificial cilia is a characteristic representation of their suitability for producing motions of all types involving any degree of deflection. By rotating the applied external magnetic field in time, the cilia are rotated through a complete $360^0$ angle at large bending angles, therefore enveloping all other possible motion profiles with smaller bending angles and degrees of rotations (Fig. 4*A*). Cilia found in nature have an additional important feature of rotating at high frequencies (e.g., one of the smallest cilia types present on medaka fish embryo beats at a frequency of around $10 - 15$ Hz) (43). A setup designed to actuate the cilia by using a conventional magnet supported on a hollow shaft is rotated at high frequencies by a direct current motor connected to the hollow shaft by a belt-drive mechanism (*SI Appendix*, Fig. S5 *A* and *B*). The hollow shaft allows for bottom illumination of cilia under the microscope as the cilia immersed in a fluid medium are best visualized in the transmission illumination mode only. The belt-drive mechanism keeps the motor at a distance, thus ensuring no interference of the motor armature magnetic field with the magnetic cilia. Microcilia with $r = 1.5$ and 1 μm and average interdistance (pitch) bigger than the cilia lengths are actuated in steps from 0 to a very high frequency of 80 Hz at extreme bending angles without the loss of motion amplitude or change in bending angle (Movies S7 and S8). Similarly, the nanocilia with $r = 350$ and 200 nm and pitches equivalent to their lengths, to minimize the magnetic interference from the neighboring cilia, are also actuated at increasing frequency steps and at large bending angles, showing no bending angle change even at the highest actuation frequencies (Movies S9 and S10). High-speed camera recordings of the high-frequency cilia rotation confirm that the phase difference between the direction of the rotating magnetic field and the cilia rotation remains limited, so that the cilia motion is

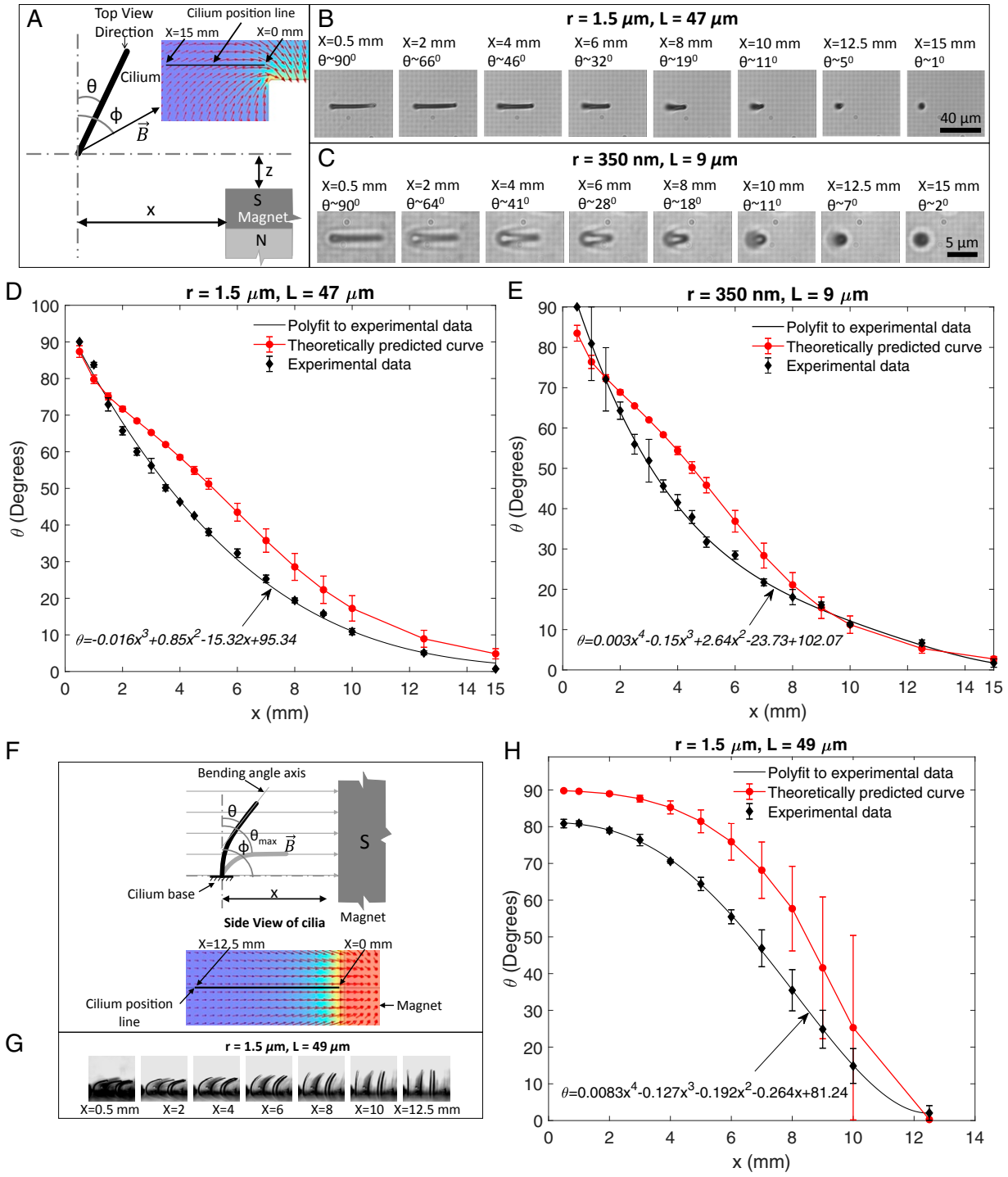


**Fig. 3.** Cilia deflection response. (*A*) Schematic representation of a cilium position with respect to a permanent magnet held at a constant $z$ position while varying its $x$ position from 15 to 0 mm. $\theta$ is the cilium deflection angle, and $\phi$ is the direction of the applied magnetic field. *Inset* illustrates the finite element simulation of the magnetic field direction due to the 7 mm cube magnet used as the external permanent magnet. (*B* and *C*) Images of a microcilium ($r = 1.5$ μm) and nanocilium ($r = 350$ nm) bending in response to various magnet positions as observed under the microscope (top view) while keeping $z$ fixed at $500 - 600$ μm. (*D* and *E*) Bending behavior from $0 - 90^0$ of the micro- and nanocilia compared with the model results (shown in Movies S1 and S2). At large bending angles, the maximum difference between the experimental data fitted with polylines ($R^2 > 0.98$) and the theoretical values is well within the 30% limit of the model accuracy. Another microcilium with $r = 1$ μm shows a similar bending behavior (*SI Appendix*, Fig. S4 and Movie S6). (*F*) Schematic representation of applied field and cilia configuration for side-view visualization while bending the cilia by moving the magnet from $x = 12.5$ mm to $x = 0.5$ mm. *Inset* shows the magnetic field direction at $z = 900$ μm extracted from a finite element model used to simulate a 7-mm cube magnet used as the external permanent magnet. (*G*) Side view of the cilia bending profile with respect to different magnet positions. The local magnetic field strengths in these images are 0.25, 0.11, 0.05, 0.028, 0.018, 0.012, and 0.009 $T$ for $x = 0.5$, 2, 4, 6, 8, 10, and 12.5 mm, respectively. (*H*) Bending behavior from $0 - 90^0$ of the microcilia compared with the model results (also shown in Movie S3). The finite element simulations were carried out with COMSOL Multiphysics software. The error bars on all the theoretically calculated values are determined by uncertainties in the values of parameters used in the theoretical model shown in *SI Appendix*, Table S1. Error bars on the experimental data are from the measurements done on multiple cilia (three to four) observed under the microscope in a particular experiment.




https://doi.org/10.1073/pnas.2104930118

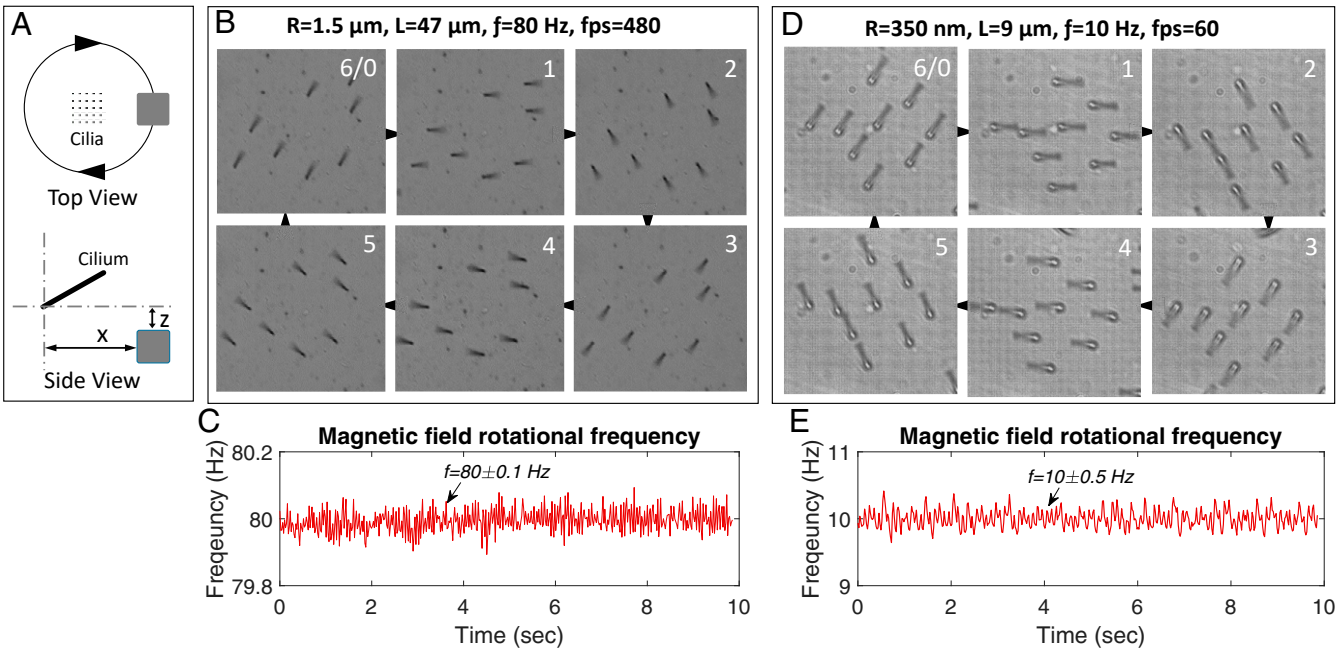


**Fig. 4.** Cilia motility response. (*A*) Schematic representation of the cilia and magnet position for $360^0$ cilia actuation. For microcilia, $x = 1.5\pm0.1$ mm and $z = 600\pm50$ µm, and for nanocilia, $x = 1.5\pm0.1$ mm and $z = 500\pm50$ µm. (*B*) Frames extracted from a video recorded at 480 fps showing in six frames a complete $360^0$ smooth and uninterrupted rotation of microcilia rotating at 80 Hz. (*C*) Readings from an encoder mounted on the motor shaft show a very stable rotating frequency of the magnet, used to actuate microcilia shown in *B*, rotated at 80 Hz with a variation of ±0.1 Hz only. (*D* and *E*) Nanocilia frames recorded at 480 frames per second (fps) showing $360^0$ rotation of nanocilia actuated at 10 Hz frequency and the corresponding stable rotating magnet frequency. Two other selected micro-/nanocilia are also recorded at high fps and frequencies (*SI Appendix*, Fig. S5 *C* and *D*).

smooth and uninterrupted (Fig. 4 *B–E*). This remarkable behavior implies that the fluid (ethanol) drag that increasingly acts on the cilia at higher frequencies to diminish motion amplitude and to introduce a phase difference (9) is dominated by the magnetic torque even at these high frequencies, indicating the strong magnetic properties of the fabricated cilia structures. Cilia with 200-nm radius are equivalent to the smallest cilia present in various biological ciliary systems like the medaka fish embryo node containing motile cilia, which are critical for determining the left–right asymmetry of the body organs (43). The absence of a model system has so far hindered their in vitro analysis and therefore, the complete understanding of the mechanism involved in establishing the asymmetry. The reported fabrication process enables, for example, mimicking the embryonic node cilia in their shape, size, distribution, and motion by creating an artificial embryonic node (Movie S11).

The limits on the size, the aspect ratio, and the geometry of the structures fabricated using the reported process are defined by the commercially available PCTE membranes used as molds. These come with pore sizes (corresponding to the cilia diameters) ranging from tens of nanometers to tens of micrometers and thicknesses (corresponding to the cilia lengths) of tens of micrometers. We used aspect ratios of 11 and 16, but our fabrication method is not fundamentally limited to the small aspect ratios, in contrast to conventional molding/demolding methods. The shapes of the PCTE membrane pores are circular, and our cilia therefore always have a circular cross-section. The experiments reported in this paper have been conducted in ethanol. The cilia can be transferred to water as long as they are not dried, and they remain equally responsive (Movie S12).

## Conclusions

The material synthesis and micro-/nanomolding fabrication process we have introduced here enables the realization of highly motile cilia with dimensions down to the sizes of their biological counterparts. This enables opportunities for implementing in vitro systems that can help us to understand the broad range of fascinating functions of the biological cilia such as those found in the embryonic nodes. Beyond this, the artificial nanocilia can be exploited to realize a variety of functions in micro- and nanodevices, such as controlled liquid pumping or mixing in micro-/nanofluidic devices, manipulation of particles and biological cells, responsive surfaces, nanorobotics, and many more.

## Materials and Methods

**Materials Used.** Materials used include reagent-grade 97% ferric chloride ($FeCl_3$), reagentPlus 98% ferrous chloride tetrahydrate ($FeCl_2 + 4H_2O$), ammonium hydroxide solution ($NH_4OH$) having 28% $NH_3$ in $H_2O$, anhydrous chloroform containing 0.5 to 1% ethanol as stabilizer, and 98% dicumyl peroxide from Sigma Aldrich. The ferric and ferrous chloride salts, being highly hygroscopic, are stored in a nitrogen glove box (Inert Laboratory 2 GB). The polymer containing 6 to 7 mol % aminopropylmethylsiloxane with dimethylsiloxane (commercial name AMS-162) was obtained from Gelest.

**Setup Design.** A setup designed to carry out the material preparation process in an inert environment consists of a $GL-45$ threaded glass bottle fitted with a leak-tight customized $GL-45$ cap to prevent the oxidation of synthesized nanomagnetic particles (*SI Appendix*, Fig. S6*A*). The cap is selected for its compatibility with glass bottles of different capacities varying from 100 mL to as high as 1 L. Fitted with a motor at its center, the cap has four transfer tubes/lines (TYGON tubes) running through it for introducing nitrogen and flushing it out, for injecting ammonium hydroxide, and for transferring the polymer into the reaction vessel. A pressure regulator between the main nitrogen supply maintained at 1 bar and the inlet tube is used to control the nitrogen flow rate into the vessel. A 10-mL burette is connected to another transfer line for dropwise injection of a given quantity of ammonium hydroxide. Each transfer line is connected with a luer lock to enable its opening and closing. A stirring rod (made from glass or polystyrene) is centrally attached to the motor shaft through a push-fit rigid coupling (made from glass or plexiglass).

**Ferrofluid Preparation.** Schematically demonstrated in Fig. 1*A*, the material synthesis process begins with preparing solutions of ferric chloride (2.43 g in 40 mL Milli-Q water) and ferrous chloride tetrahydrate (1.49 g in 40 mL Milli-Q water) in 2 : 1 molar concentration, which are then poured into

the glass bottle. Closed with the $GL-45$ cap, the bottle is flushed with nitrogen for half an hour as the stirrer is turned on, and the rotating rate is maintained at around 600 rpm. The solution is now titrated with a minimal quantity ($\sim$ 4 ml) of ammonium hydroxide solution to reach the equivalence point, on the characteristic pH graph (*SI Appendix*, Fig. S6*B*), to completely precipitate the nanomagnetic particles (magnetite). The total quantity of magnetic particles synthesized is calculated by balancing the chemical reaction involved in the particle synthesize (44). After a waiting time of 10 to 15 minutes, a sufficient quantity (4 mL) of the polymer is added and stirred for another half an hour. More ammonium hydroxide is now added to raise the pH near to 12, and all the transfer lines are closed. The leak-tight cap and closed valves ensure a near-inert environment for a long-enough time while the stirring is continued overnight to facilitate the particle–polymer binding. Apart from maintaining an inert environment, closing of the transfer lines is required to suppress the fluid evaporation, which otherwise reduces the solution pH and results into transformation of the fluid into two separate phases—a clear aqueous phase and a thick black particle–polymer mixture. Separation into two phases is a condition to be avoided for the maximum binding of particles with the polymer.

To extract the coated and uncoated particles from the extra polymer, after overnight stirring, the particles are first settled on a permanent magnet, leaving a clear aqueous phase above. Decanting the aqueous phase, the particles are washed twice in methanol, two times by water, and then again twice with methanol. Each time, the solution is stirred for a few minutes with a glass rod, and the particles are again settled using a permanent magnet to remove the solvents. We observed that for complete removal of the extra polymer, a large quantity of methanol ($\sim$ 200 ml) should be used in the first step of the washing process. The washed content is now mixed with chloroform ($\sim$ 20 ml) and sonicated for half an hour, forming a stable solution of the coated particles and the solvent. The solution is transferred to 15-ml vials, and the uncoated particles are settled on a permanent magnet by allowing a settle time of around 1 h before the solution is transferred to new vials. A small quantity (0.5 to 1 ml) of the solution is used to find the exact percentage of coated particles present by weighing the sample before and after the chloroform evaporation. Concentration tuning is done by adding a calculated amount of polymer along with the curing agent dicumyl peroxide in a 1 : 10 ratio, and the solution is again sonicated for half an hour. Evaporating the chloroform leaves behind a thick paste of the polymer containing homogeneously dispersed nanomagnetic particles. The fluid can further be cured in a vacuum heat oven to yield a magnetic elastomer material as mentioned above and also described in detail in *SI Appendix*, Text S1 and Fig. S1.

**Data Availability.** All study data are included in the article and/or supporting information.

**ACKNOWLEDGMENTS.** The devices were prepared in the Microfab laboratory at Eindhoven University of Technology and processed in the Polymer Technology laboratory at TU/e. Material magnetization tests and device preparation for scanning electron microscopy imaging were done in the Nanolab@tue. The work is funded by European Union's Horizon 2020 Research and Innovation Programme under Marie Sklodowska-Curie Grant 754462 and the European Research Council–funded Project Bio-Plan under Advanced Grant Physical Sciences and Engineering 8, 2018, Grant 833214.



1. E. F. Smith, R. Rohatgi, Cilia 2010: The surprise organelle of the decade. *Sci Signal* **4**, mr1 (2011).
2. W. Gilpin, M. S. Bull, M. Prakash, The multiscale physics of cilia and flagella. *Nat. Rev. Phys.* **2**, 74–88 (2020).
3. M. Delling, P. G. DeCaen, J. F. Doerner, S. Febvay, D. E. Clapham, Primary cilia are specialized calcium signalling organelles. *Nature* **504**, 311–314 (2013).
4. A. S. Shah, Y. Ben-Shahar, T. O. Moninger, J. N. Kline, M. J. Welsh, Motile cilia of human airway epithelia are chemosensory. *Science* **325**, 1131–1134 (2009).
5. J. den Toonder *et al*., Artificial cilia for active micro-fluidic mixing. *Lab Chip* **8**, 533–541 (2008).
6. F. Fahrni, M. W. Prins, L. J. van Ijzendoorn, Micro-fluidic actuation using magnetic artificial cilia. *Lab Chip* **9**, 3413–3421 (2009).
7. M. Vilfan *et al*., Self-assembled artificial cilia. *Proc. Natl. Acad. Sci. U.S.A.* **107**, 1844–1847 (2010).
8. S. N. Khaderi *et al*., Magnetically-actuated artificial cilia for microfluidic propulsion. *Lab Chip* **11**, 2002–2010 (2011).
9. Y. Wang, Y. Gao, H. Wyss, P. Anderson, J. den Toonder, Out of the cleanroom, self-assembled magnetic artificial cilia. *Lab Chip* **13**, 3360–3366 (2013).
10. C.-Y. Chen, C.-Y. Chen, C.-Y. Lin, Y.-T. Hu, Magnetically actuated artificial cilia for optimum mixing performance in microfluidics. *Lab Chip* **13**, 2834–2839 (2013).
11. S. Zhang, Y. Wang, R. Lavrijsen, P. R. Onck, J. M. J. den Toonder, Versatile microfluidic flow generated by moulded magnetic artificial cilia. *Sens. Actuators B Chem.* **263**, 614–624 (2018).
12. S. Hanasoge, P. J. Hesketh, A. Alexeev, Microfluidic pumping using artificial magnetic cilia. *Microsyst. Nanoeng.* **4**, 1–9 (2018).
13. K. E. Peyer, L. Zhang, B. J. Nelson, Bio-inspired magnetic swimming microrobots for biomedical applications. *Nanoscale* **5**, 1259–1272 (2013).
14. A. Bhattacharya, G. A. Buxton, O. B. Usta, A. C. Balazs, Propulsion and trapping of microparticles by active cilia arrays. *Langmuir* **28**, 3217–3226 (2012).
15. S. Zhang, Y. Wang, P. R. Onck, J. M. J. den Toonder, Removal of microparticles by ciliated surfaces—an experimental study. *Adv. Funct. Mater.* **29**, 1806434 (2019).
16. Y. Zhu, D. S. Antao, R. Xiao, E. N. Wang, Real-time manipulation with magnetically tunable structures. *Adv. Mater.* **26**, 6442–6446 (2014).
17. D.-M. Drotlef, P. Blümler, A. del Campo, Magnetically actuated patterns for bioinspired reversible adhesion (dry and wet). *Adv. Mater.* **26**, 775–779 (2014).
18. J. M. J. den Toonder, P. R. Onck, Microfluidic manipulation with artificial/bioinspired cilia. *Trends Biotechnol.* **31**, 85–91 (2013).
19. X. Pang, J. Lv, C. Zhu, L. Qin, Y. Yu, Photodeformable azobenzene-containing liquid crystal polymers and soft actuators. *Adv. Mater.* **31**, 1904224 (2019).
20. M. Li, T. Kim, G. Guidetti, Y. Wang, F. G. Omenetto, Optomechanically actuated microcilia for locally reconfigurable surfaces. *Adv. Mater.* **32**, 2004147 (2020).
21. B. Gorissen, M. de Volder, D. Reynaerts, Pneumatically-actuated artificial cilia array for biomimetic fluid propulsion. *Lab Chip* **15**, 4348–4355 (2015).
22. S. Orbay, A. Ozcelik, H. Bachman, T. J. Huang, Acoustic actuation of in situ fabricated artificial cilia. *J. Micromech. Microeng.* **28**, 025012 (2018).
23. K. Oh, J.-H. Chung, S. Devasia, J. J. Riley, Bio-mimetic silicone cilia for microfluidic manipulation. *Lab Chip* **9**, 1561–1566 (2009).
24. A. Keißner, C. Brücker, Directional fluid transport along artificial ciliary surfaces with base-layer actuation of counter-rotating orbital beating patterns. *Soft Matter* **8**, 5342–5349 (2012).
25. B. A. Evans *et al*., Magnetically actuated nanorod arrays as biomimetic cilia. *Nano Lett.* **7**, 1428–1434 (2007).
26. R. M. Judith *et al*., Micro-elastometry on whole blood clots using actuated surface-attached posts (asaps). *Lab Chip* **15**, 1385–1393 (2015).
27. Z. Luo, X. A. Zhang, B. A. Evans, C. H. Chang, Active periodic magnetic nanostructures with high aspect ratio and ultrahigh pillar density. *ACS Appl. Mater. Interfaces* **12**, 11135–11143 (2020).
28. A. R. Shields *et al*., Biomimetic cilia arrays generate simultaneous pumping and mixing regimes. *Proc. Natl. Acad. Sci. U.S.A.* **107**, 15670–15675 (2010).
29. F. Qiu *et al*., Bio-inspired microrobots. *Mater. Today* **15**, 463 (2012).
30. L. Fischer, A. M. Menzel, Magnetostriction in magnetic gels and elastomers as a function of the internal structure and particle distribution. *J. Chem. Phys.* **151**, 114906 (2019).
31. Y. Li, J. Li, W. Li, H. Du, A state-of-the-art review on magnetorheological elastomer devices. *Smart Mater. Struct.* **23**, 123001 (2014).
32. Z. Rigbi, L. Jilken, The response of an elastomer filled with soft ferrite to mechanical and magnetic influences. *J. Magn. Magn. Mater.* **37**, 267–276 (1983).
33. M. R. Jolly, J. D. Carlson, B. C. Muñoz, T. A. Bullions, The magnetoviscoelastic response of elastomer composites consisting of ferrous particles embedded in a polymer matrix. *J. Intell. Mater. Syst. Struct.* **7**, 613–622 (1996).
34. R. Elhajjar, C.-T. Law, A. Pegoretti, Magnetostrictive polymer composites: Recent advances in materials, structures and properties. *Prog. Mater. Sci.* **97**, 204–229 (2018).
35. S. Zhang, R. Zhang, Y. Wang, P. R. Onck, J. M. J. den Toonder, Controlled multidirectional particle transportation by magnetic artificial cilia. *ACS Nano* **14**, 10313–10323 (2020).
36. F. Fahrni, M. W. J. Prins, L. J. Van IJzendoorn, Magnetization and actuation of polymeric microstructures with magnetic nanoparticles for application in microfluidics. *J. Magn. Magn. Mater.* **321**, 1843–1850 (2009).
37. B. A. Evans *et al*., A highly tunable silicone-based magnetic elastomer with nanoscale homogeneity. *J. Magn. Magn. Mater.* **324**, 501–507 (2012).
38. Z. Luo, B. A. Evans, C. H. Chang, Magnetically actuated dynamic iridescence inspired by the neon tetra. *ACS Nano* **13**, 4657–4666 (2019).
39. L. Kong *et al*., Self-adaptive magnetic photonic nanochain cilia arrays. *Adv. Funct. Mater.* **30**, 2005243 (2020).
40. R. Massart, Preparation of aqueous magnetic liquids in alkaline and acidic media. *IEEE Trans. Magn.* **17**, 1247–1248 (1981).
41. J. N. Lee, C. Park, G. M. Whitesides, Solvent compatibility of poly(dimethylsiloxane)-based microfluidic devices. *Anal. Chem.* **75**, 6544–6554 (2003).
42. J. J. Abbott, O. Ergeneman, M. P. Kummer, A. M. Hirt, B. J. Nelson, Modeling magnetic torque and force for controlled manipulation of soft-magnetic bodies. *IEEE Trans. Robot.* **23**, 1247–1252 (2007).
43. Y. Okada, S. Takeda, Y. Tanaka, J. I. Belmonte, N. Hirokawa, Mechanism of nodal flow: A conserved symmetry breaking event in left-right axis determination. *Cell* **121**, 633–644 (2005).
44. M. Widdrat, "Formation and alteration of magnetite nanoparticles," PhD thesis, Universität Potsdam, Mathematisch-Naturwissenschaftliche Fakultät, Potsdam, Germany (2014).